

INORGANIC CHEMISTRY

FRONTIERS



CHINESE
CHEMICAL
SOCIETY



ROYAL SOCIETY
OF CHEMISTRY

rsc.li/frontiers-inorganic

RESEARCH ARTICLE

[View Article Online](#)
[View Journal](#) | [View Issue](#)



Cite this: *Inorg. Chem. Front.*, 2023, **10**, 1721

Topological control of metal–organic frameworks toward highly sensitive and selective detection of chromate and dichromate†

Zi-Jian Li, ^a Yu Ju, ^{a,c} Xiao-Ling Wu, ^a Xiaoyun Li, ^a Jie Qiu, ^b Yongxin Li, ^d Zhi-Hui Zhang, ^c Ming-Yang He, ^c Linjuan Zhang, ^a Jian-Qiang Wang ^a and Jian Lin ^{a,b}

Luminescent metal–organic frameworks (LMOFs) have been extensively used as sensitive and selective sensors for carcinogenic chromium(vi) oxyanions. However, the correlation between the MOF structure and the Cr(vi) sensing efficacy remains underexplored, hindering the rational design of MOFs for Cr(vi) sensing. Herein, we overcome this challenge by judiciously selecting the rarely touched thorium cations and a tetraphenylethene-based ligand for building two novel thorium-based MOFs, **Th-BCTPE-1** and **Th-BCTPE-2**. Despite being built from identical precursors, **Th-BCTPE-1** shows more sensitive luminescence quenching responses to CrO_4^{2-} and $\text{Cr}_2\text{O}_7^{2-}$ than **Th-BCTPE-2**, producing the second highest quenching constants of CrO_4^{2-} among all LMOF-based Cr(vi) sensors. We further decoupled the influences of different structural variables and the corresponding physiochemical properties, including porosity, BET surface area, photoluminescence quantum yield, and adsorption capacity, showing that the sensing efficacy of Cr(vi) oxyanions is more relevant to the adsorption capacity and the degree of the inner filter effect than the rest of the variables in this system.

Received 10th December 2022,
Accepted 30th December 2022

DOI: 10.1039/d2qi02631g

rsc.li/frontiers-inorganic

Introduction

Chromates and dichromates have been extensively used to improve the corrosion resistance of active metals *via* the formation of stable chromate conversion coating.¹ Moreover, Cr(vi) oxyanions are essential in advanced nuclear cycles since chromate and dichromate have been used as corrosion inhibitors in cooling water for nuclear reactors.^{2,3} Cooling water with an approximate Cr(vi) concentration of $700 \text{ }\mu\text{g kg}^{-1}$ is discharged from the reactors to natural water bodies after cooling in retention basins.⁴ As a consequence, high-level Cr(vi) contamination (ranging up to nearly 300 mg kg^{-1}) has been identified in the groundwater at the Hanford site and the nearby

Columbia river, which imposes a potential hazard to human health due to its high carcinogenicity.^{4,5} Furthermore, the presence of chromate in high-level waste (HLW) leads to the formation of undesirable spinel crystals during the vitrification of nuclear waste, which increases the anticipated cost and risk of HLW vitrification.⁶ Hence, facile detection and the subsequent effective sequestration of chromate and dichromate from contaminated water and HLW are highly indispensable.^{7–11} The concentration of Cr(vi) solution can be determined colorimetrically by the diphenylcarbazide method.⁴ However, this technology suffers from low sensitivity (limit of detection of 0.5 mg kg^{-1}). Instrumental techniques including inductively coupled plasma atomic emission spectroscopy (ICP-AES) and inductively coupled plasma mass spectrometry (ICP-MS) are advantageous in terms of limit of detection (LOD)¹² but they are unable to distinguish the toxic Cr(vi) from the benign Cr(III) ion, the latter of which is the dominant natural background species of chromium in sediments.

As a class of porous inorganic–organic hybrid materials, metal–organic frameworks (MOFs) are scientifically compelling and functionally evolving with considerable advances made in various fields including separation, sensing, and catalysis.^{13–18} Incorporating luminescent metal nodes and/or organic linkers within MOFs engenders the sensing capacities of MOFs in a turn-off, turn-on, or fluorochromic manner, making them suitable for chromate/dichromate sensing.^{19–22}

^aKey Laboratory of Interfacial Physics and Technology, Shanghai Institute of Applied Physics, Chinese Academy of Sciences, Shanghai 201800, China

^bSchool of Nuclear Science and Technology, Xi'an Jiaotong University, No. 28, West Xianning Road, Xi'an, 710049, P. R. China. E-mail: jianlin@xjtu.edu.cn

^cJiangsu Key Laboratory of Advanced Catalytic Materials and Technology, Changzhou University, Changzhou 213164, China

^dDivision of Chemistry and Biological Chemistry, School of Physical and Mathematical Sciences, Nanyang Technological University, 637371, Singapore

† Electronic supplementary information (ESI) available: PXRD, TGA, excitation and PL spectra, photoluminescence lifetimes, quenching rates, SEM-EDS, and crystallographic data. CCDC 2213561 and 2213562. For ESI and crystallographic data in CIF or other electronic format see DOI: <https://doi.org/10.1039/d2qi02631g>

Furthermore, the highly tunable compositions, structures, and pore functionalities of MOFs give rise to a series of chromate/dichromate sensors with high sensitivity and excellent selectivity.^{23–28} Although significant progress in the development of MOFs for Cr(vi) detection has been achieved, understanding the relationship between the MOF structure and the sensing efficacy remains in its infancy, which hinders the rational design of MOFs for Cr(vi) sensing. The study by Sun and coworkers indicated that modifying the pore shape and volume of MOFs *via* altering the linker shape have a notable influence on the detection sensitivity of dichromate.²⁵ Moreover, a mixed-ligand strategy gave rise to three cadmium coordination polymers, of which the one-dimensional polymer exhibited the best sensing performance.²⁹ However, both the organic linkers and the topologies of MOFs are changed in these systems, rendering the decoupling of the influence of each variable on the luminescence properties rather difficult. Therefore, an outstanding challenge in obtaining the structure–property correlation is to alter the underlying topologies of MOFs without introducing additional variables.

We have recently undertaken a study on the control of the polymorphism of MOFs by utilizing thorium-based metal–organic frameworks (Th-MOFs) as a platform.³⁰ One of the key merits of Th-MOFs is that the appropriate “hardness” of Th⁴⁺ can afford different secondary building units (SBUs) with a wide range of nuclearity and correspondingly diverse topologies.^{31–35} Besides, the Th⁴⁺ cation typically adopts a nine-coordinate capped square antiprism geometry, which provides an additional coordinating site on its capping addenda for creating new structures.^{36–39} This can be exemplified by a series of Th-MOFs that feature five unique topologies even though they are built from the same 2'-methyl-[1,1':4',1"-terphenyl]-4,4"-dicarboxylate (MeTPDC²) ligand.³⁸ Such topological polymorphism of Th-MOFs facilitates a better understanding of how the structure of MOF, in isolation, influences the sensing efficacy of Cr(vi) oxyanions.

Herein, we showcase a synthetic modulation approach to obtain two topologically distinct Th-MOFs, [Th₆(OH)₄(O)₄(H₂O)₆](BCTPE)₆·(DMF)₁₈·(H₂O)₉ (**Th-BCTPE-1**) and [Th₆(OH)₄(O)₄(H₂O)₆](BCTPE)₅(HCOO)₂·(DMF)₂₆·(H₂O)₃₂ (**Th-BCTPE-2**), built from the same (E)-4,4'-(1,2-diphenylethene-1,2-diyl)dibenzoate linker (BCTPE²⁻). As a π -electron-rich dicarboxylate ligand, H₂BCTPE was used as a fluorophore to engender the luminometric sensing capacities of **Th-BCTPE-1** and **Th-BCTPE-2** for chromate and dichromate. Notably, the UiO-type MOF **Th-BCTPE-1** features greater quenching constants (K_{SV}) and a lower limit of detection (LOD) than **Th-BCTPE-2** for both chromate and dichromate. The polymorphism of these Th-MOFs and the corresponding different sensing efficacies show the profound effect of structure on Cr(vi) sensing and shed light on the future rational design of highly efficient Cr(vi) sensors.

Results and discussion

By modifying the stoichiometry, modulator, and reaction temperature, solvothermal reactions between the identical pre-

ursors of Th(NO₃)₄·6H₂O and (E)-4,4'-(1,2-diphenylethene-1,2-diyl)dibenzoic acid (H₂BCTPE) allow for the isolation of two different Th-MOFs, **Th-BCTPE-1** and **Th-BCTPE-2**. When trifluoroacetic acid was selected as a modulator, a reaction at 80 °C gave rise to octahedral single-crystals of **Th-BCTPE-1** (Fig. S1a†). Incorporating nitric acid in the synthesis at 120 °C resulted in the crystallization of prismatic crystals of **Th-BCTPE-2** (Fig. S1b†).

Single-crystal X-ray diffraction (SCXRD) study revealed that **Th-BCTPE-1** adopts a typical UiO type structure with the cubic *Fm*3*m* space group and fcu topology (Table S1†). The asymmetric unit of its framework is composed of one crystallographically unique 1/8 Th⁴⁺, 1/6 μ_3 -OH/ μ_3 -O, 1/8 coordinating H₂O (1/48 [Th₆(μ_3 -OH)₄(μ_3 -O)₄(H₂O)₆]¹²⁺), and 1/8 BCTPE²⁻. As shown in Fig. 1a, the secondary building unit (SBU) of **Th-BCTPE-1** is built from six Th cations interconnected by four μ_3 -OH and four μ_3 -O groups and further decorated by six H₂O molecules. The afforded [Th₆(μ_3 -OH)₄(μ_3 -O)₄(H₂O)₆]¹²⁺ cluster is bridged by twelve BCTPE²⁻ dicarboxylate linkers with the neighbouring clusters, generating a 12-connected SBU. Two types of voids, namely an octahedral (9.0 Å) and a tetrahedral (6.2 Å) void, were identified. These cavities are occupied by disordered DMF and H₂O guest species, accounting for a total volume of 34.1% as estimated by PLATON.⁴⁰

Th-BCTPE-2 crystallizes in the *P4*₂/mmc space group and its asymmetric unit is assembled from one 1/8 Th₆(μ_3 -OH)₄(μ_3 -O)₄(H₂O)₆(HCOO)₂ cluster, one 1/2 and one 1/8 BCTPE²⁻ anion. In sharp contrast to **Th-BCTPE-1**, the SBU of **Th-BCTPE-2** is assembled from a [Th₆(μ_3 -OH)₄(μ_3 -O)₄(H₂O)₆]¹²⁺ core chelated with ten BCTPE²⁻ ligands and two HCOO⁻ anions (Fig. 1b). It is worth noting that HCOO⁻ anions originated from the hydrolyzation of DMF molecules in the presence of nitric acid with extended reaction time. Unlike the bitopic BCTPE²⁻ ligands that interconnect the neighbouring Th₆ SBUs, the HCOO⁻ groups in **Th-BCTPE-2** terminate the bridging of SBUs. Thus, each Th₆ SBU is connected to ten neighbouring ones, giving a final three-dimensional porous network with the bcu topology. Such a structure renders open channels of approximately 8.1 Å × 8.1 Å, that result in a much higher solvent-accessible volume of 64.7% than that of **Th-BCTPE-1**.

Th-BCTPE-1 and **Th-BCTPE-2** can be obtained as pure phases, as confirmed by the similar powder X-ray diffraction (PXRD) patterns of the as-synthesized samples and the simulated ones (Fig. S2†). The permanent porosities of these Th-MOFs were examined by N₂ adsorption/desorption isotherms measured at 77 K. Both **Th-BCTPE-1** and **Th-BCTPE-2** exhibited typical type I isotherms with saturated uptakes of 69.8 and 115.4 cm³ g⁻¹, respectively, corresponding to Brunauer–Emmett–Teller (BET) surface areas of 188 and 316 m² g⁻¹ (Fig. 2). This trend matches well with the tendency of void volumes obtained from PLATON. The desorption branches of both materials feature slight hysteresis loops, which are characteristic of moderate interactions between N₂ and the frameworks. Thermogravimetric analysis (TGA) study revealed that **Th-BCTPE-1** and **Th-BCTPE-2** are stable up to 490 and

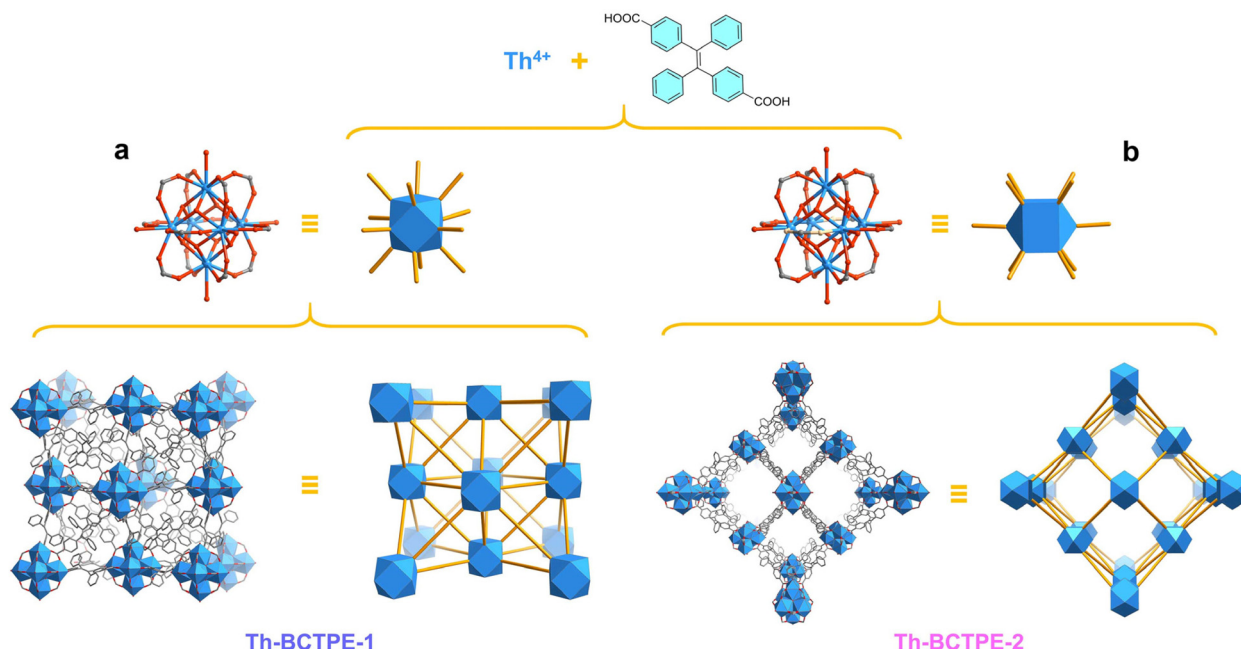


Fig. 1 (a) The 12-connected $\text{Th}_6(\mu_3\text{-OH})_4(\mu_3\text{-O})_4(\text{H}_2\text{O})_6(\text{R-COO})_{12}$ SBU, 3D structure, and simplified topology of **Th-BCTPE-1**. (b) The 10-connected $\text{Th}_6(\mu_3\text{-OH})_4(\mu_3\text{-O})_4(\text{H}_2\text{O})_6(\text{HCOO})_2(\text{R-COO})_{10}$ SBU, 3D structure, and simplified topology of **Th-BCTPE-2**. Colour code: Th atoms are shown in blue, O atoms are in red, C atoms from the BCTPE²⁻ ligands are in grey, and O atoms from the HCOO⁻ ligand are in light yellow.

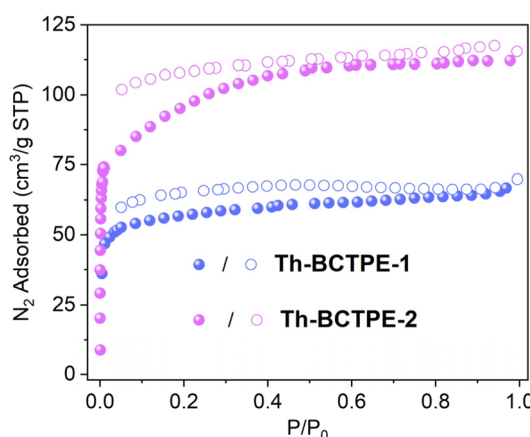


Fig. 2 N_2 adsorption/desorption isotherms of **Th-BCTPE-1** and **Th-BCTPE-2** at 77 K.

510 °C, respectively (Fig. S3†). Both Th-MOFs undergo three stages of weight loss, and the first and second stages correspond to the departure of guest species including DMF and H_2O . **Th-BCTPE-2** features a greater amount of solvent loss ($w\% = 39.9\%$) due to its larger void space than that of **Th-BCTPE-1**.

Despite the tremendous effort focused on the aggregation-induced emission (AIE) of tetraphenylethene, there has been only one MOF report to date integrating the BCTPE²⁻ ligand, a dicarboxylate derivative of TPE.⁴¹ The luminescence properties of **Th-BCTPE-1** and **Th-BCTPE-2** were initially investigated by collecting their emission spectra. Upon 365 nm UV excitation,

Th-BCTPE-1 and **Th-BCTPE-2** exhibit green luminescence with emission bands centered at 495 and 500 nm, respectively, which are red-shifted in comparison with the blue emission ($\lambda_{\text{max}} = 467$ nm) of the pure H_2BCTPE ligand (Fig. S4†). The luminescence of these Th-MOFs can be ascribed to the matrix coordination-induced emission (MCIE), whereas that of H_2BCTPE could result from the AIE effect.⁴² Moreover, the photoluminescence quantum yields (PLQYs) under ambient conditions were measured to be 50.53% and 53.07% for **Th-BCTPE-1** and **Th-BCTPE-2**, respectively, both of which are higher than 39.19% for H_2BCTPE . This observation indicates that the ordered and spatial anchoring of fluorescent BCTPE²⁻ moieties inside rigid Th-MOFs can efficiently eliminate possible dissipative processes and turn on fluorescence.^{43–45} In addition, **Th-BCTPE-1**, **Th-BCTPE-2** and H_2BCTPE show bi-exponential luminescence decays with average lifetimes of 3.21, 2.45, and 2.87 ns, respectively (Fig. S5†).

Given the intense emissions and high PLQYs of both materials, we sought to investigate the potential utility of **Th-BCTPE-1** and **Th-BCTPE-2** for chromate and dichromate sensing. Moreover, their variety and multiplicity in terms of structures, void spaces, and surface areas make them ideal candidates for elucidating the correlations of the MOF structure with the Cr(vi) sensing efficacy. In this regard, equivalent amounts (0.16 μmol) of **Th-BCTPE-1** or **Th-BCTPE-2** were dispersed in 2 mL K_2CrO_4 or $\text{K}_2\text{Cr}_2\text{O}_7$ solution with increasing concentrations. Both **Th-BCTPE-1** and **Th-BCTPE-2** were finely ground to make the materials homogeneously dispersed in Cr(vi) solutions and to eliminate the effect of morphology difference. As shown in Fig. 3, the emissions of both Th-MOFs

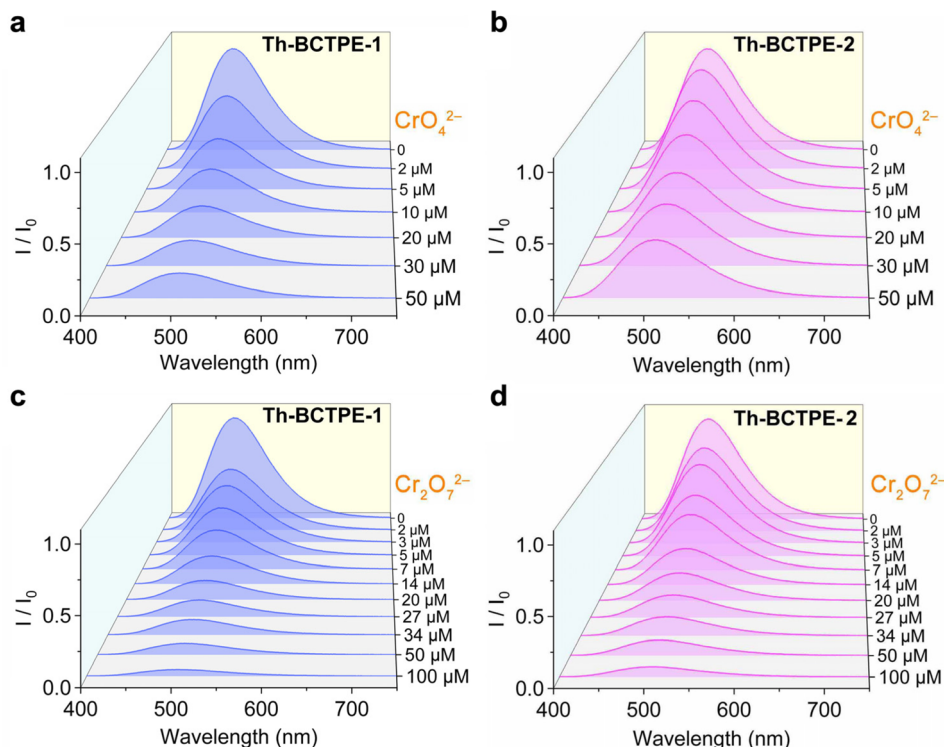


Fig. 3 Normalized luminescence spectra of (a) Th-BCTPE-1 as a function of increasing CrO_4^{2-} concentration, (b) Th-BCTPE-2 as a function of increasing CrO_4^{2-} concentration, (c) Th-BCTPE-1 as a function of increasing $\text{Cr}_2\text{O}_7^{2-}$ concentration, and (d) Th-BCTPE-2 as a function of increasing $\text{Cr}_2\text{O}_7^{2-}$ concentration.

were gradually quenched upon increasing the addition of CrO_4^{2-} or $\text{Cr}_2\text{O}_7^{2-}$ and differences in the sensing efficacy of CrO_4^{2-} can be resolved between the two Th-MOFs. Specifically, the addition of 50 μM CrO_4^{2-} resulted in 88.1% and 58.0% decreases in the luminescence intensities of Th-BCTPE-1 and Th-BCTPE-2, respectively, suggesting that Th-BCTPE-2 is more robust against quenching than Th-BCTPE-1 (Fig. 4a). To gain deeper insight into the quenching behaviours, the quenching constants (K_{SV}) in the lower concentration range (0.1–1 μM) were derived from the Stern–Volmer (S–V) plots, $I_0/I = 1 + K_{\text{SV}}[Q] - 1$, where $[Q]$ is the concentration of the quencher, and I_0 and I are emission intensities before and after adding quenchers, respectively.⁴⁶ As shown in Fig. 4b, the S–V plots for Th-BCTPE-1 and Th-BCTPE-2 are linear in the range of 0.1–1 μM and downward deviations from the linear dependence occur at higher concentrations for both materials. The K_{SV} values were calculated to be $2.4(1) \times 10^5$ and $1.30(7) \times 10^5 \text{ M}^{-1}$ for Th-BCTPE-1 and Th-BCTPE-2, respectively, which is indicative of the higher sensing efficacy of Th-BCTPE-1 than that of Th-BCTPE-2. Notably, the K_{SV} of Th-BCTPE-1 for CrO_4^{2-} is the second highest among all MOF-based chemosensors (Table S2†).⁴⁷ The limits of detection (LODs) were calculated to be 9.0 and 159 nM ($3\sigma/k$) for Th-BCTPE-1 and Th-BCTPE-2, respectively, which agree well with that of K_{SV} (Table S3†).⁴⁸

Aligned with the CrO_4^{2-} sensing, the sensing capacities of Th-BCTPE-1 and Th-BCTPE-2 for $\text{Cr}_2\text{O}_7^{2-}$ were also investigated, showing that their difference in $\text{Cr}_2\text{O}_7^{2-}$ sensing efficacy

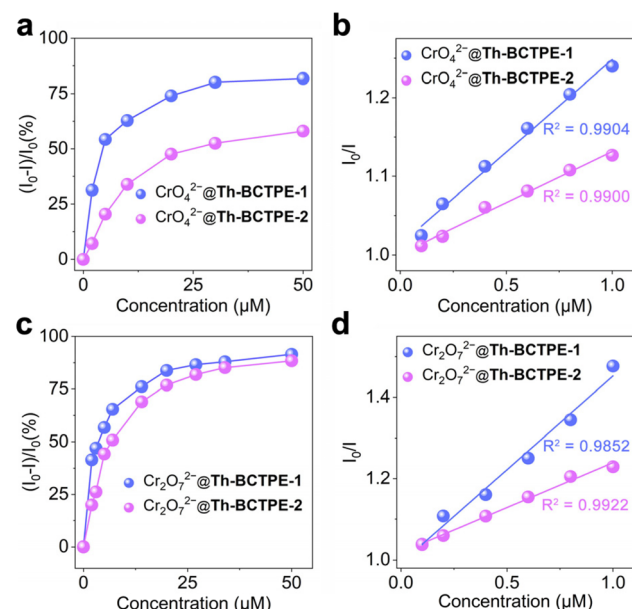


Fig. 4 (a) The quenching rates of Th-BCTPE-1 and Th-BCTPE-2 as a function of CrO_4^{2-} concentration. (b) Stern–Volmer plots of luminescence quenching of Th-BCTPE-1 and Th-BCTPE-2 in CrO_4^{2-} solution. (c) The quenching rates of Th-BCTPE-1 and Th-BCTPE-2 as a function of $\text{Cr}_2\text{O}_7^{2-}$ concentration. (d) Stern–Volmer plots of luminescence quenching of Th-BCTPE-1 and Th-BCTPE-2 in $\text{Cr}_2\text{O}_7^{2-}$ solution.

is relatively trivial in the concentration range of 0–50 μM (Fig. 4c). However, the quenching rate of **Th-BCTPE-1** is much faster than that of **Th-BCTPE-2** in a lower concentration range as shown in (Fig. S6†), suggesting that **Th-BCTPE-2** is more quenching-resistant to $\text{Cr}_2\text{O}_7^{2-}$ than **Th-BCTPE-1**. In a similar vein, the quenching constants for $\text{Cr}_2\text{O}_7^{2-}$ were acquired from the S-V plots, showing a higher K_{SV} ($4.6(3) \times 10^5 \text{ M}^{-1}$) of **Th-BCTPE-1** than $2.222(9) \times 10^5 \text{ M}^{-1}$ of **Th-BCTPE-2**. **Th-BCTPE-1** again exhibited a higher sensing efficacy for $\text{Cr}_2\text{O}_7^{2-}$ than **Th-BCTPE-2** (Fig. 4d). Moreover, the LODs for $\text{Cr}_2\text{O}_7^{2-}$ were derived from the linear regression analysis and calculated to be 4.6 and 94 nM for **Th-BCTPE-1** and **Th-BCTPE-2**, respectively, whose trend agrees well with those for CrO_4^{2-} .

Besides the quenching efficacies, the adsorption capacities of **Th-BCTPE-1** and **Th-BCTPE-2** for Cr(vi) oxyanions were also comparatively investigated. Scanning electron microscopy and energy dispersive X-ray spectroscopy (SEM-EDS) revealed that Cr was homogeneously dispersed on the surface of CrO_4^{2-} –

and $\text{Cr}_2\text{O}_7^{2-}$ –soaked crystals (Fig. S7†). Moreover, the sorption isotherms indicated that both **Th-BCTPE-1** and **Th-BCTPE-2** can capture CrO_4^{2-} and $\text{Cr}_2\text{O}_7^{2-}$ anions. The uptake of anionic CrO_4^{2-} and $\text{Cr}_2\text{O}_7^{2-}$ by neutral **Th-BCTPE-1** and **Th-BCTPE-2** could be largely attributed to the electrostatic interactions between cationic SBUs and anions.^{38,49,50} The sorption isotherms can be better fitted with the Langmuir model than the Freundlich model (Table S4†). Notably, **Th-BCTPE-1** featured higher maximum uptake capacities of CrO_4^{2-} and $\text{Cr}_2\text{O}_7^{2-}$ (1.58 and 1.05 mol mol⁻¹) than those of **Th-BCTPE-2** (1.22 and 0.93 mol mol⁻¹) (Fig. 5a and b). This observation appears to be counterintuitive at first glance since **Th-BCTPE-2** has a greater void volume and a larger BET surface area than those of **Th-BCTPE-1**. However, a recent study by us revealed that the high porosity of MOFs cannot guarantee high adsorption capacity.⁵¹ Since **Th-BCTPE-1** incorporates fewer solvent species, its open void is more accessible than **Th-BCTPE-2**, which renders **Th-BCTPE-1** a more efficient absorbent for both CrO_4^{2-} and $\text{Cr}_2\text{O}_7^{2-}$.

Elucidating the correlation between the structure of MOF and the sensing efficacy of Cr(vi) oxyanions is essential to the rational design of new chemosensors.^{52–54} Therefore, structural and photophysical parameters, including void volumes, BET surface areas, PLQYs, K_{SV} values, and LODs, as well as the maximum adsorption capacities, are summarized in Table 1. As seen, the porosity, surface area, and PLQY are not necessarily relevant to the sensing efficacy. In contrast, the trend of maximum adsorption capacity is in line with that of K_{SV} , implying that the sensing efficacy could be more strongly associated with Cr(vi) adsorption. Indeed, additional insights into the correlation between the sensing efficacy and sorption capacity can be derived from the S-V plots extending to higher a concentration range (Fig. S8†). For both CrO_4^{2-} and $\text{Cr}_2\text{O}_7^{2-}$ sensing, **Th-BCTPE-1** showed saturation plateaus at higher concentrations than **Th-BCTPE-2**. These observations conjointly suggest that the luminophores of **Th-BCTPE-1** are more accessible to CrO_4^{2-} and $\text{Cr}_2\text{O}_7^{2-}$ than those of **Th-BCTPE-2**, which could be largely ascribed to the higher adsorption capacities of **Th-BCTPE-1** for Cr(vi) oxyanions. In addition, a UV-vis absorption spectroscopy study revealed that the spectra of K_2CrO_4 and $\text{K}_2\text{Cr}_2\text{O}_7$ exhibit two intense absorption peaks at 230–310 nm and 310–450 nm, both of which overlap with the excitation spectra of **Th-BCTPE-1** and **Th-BCTPE-2** (Fig. S9†). Consequently, the emission intensity reduction and eventual luminescence quenching upon titration of chromium oxyanions can be attributed to a strong inner filter effect.^{55–57} More importantly, the overlap efficacy between the excitation

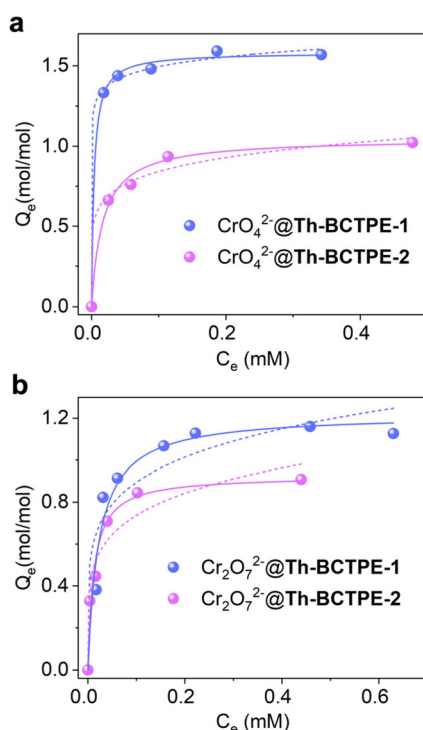


Fig. 5 Adsorption isotherms of **Th-BCTPE-1** and **Th-BCTPE-2** for (a) CrO_4^{2-} and (b) $\text{Cr}_2\text{O}_7^{2-}$ fitted with the Langmuir model (solid line) and the Freundlich model (dashed line).

Table 1 The void volumes, BET surface areas, photoluminescence quantum yields, K_{SV} values, LODs, and maximum adsorption capacities of **Th-BCTPE-1** and **Th-BCTPE-2**

Products	Void (%)	BET surface area ($\text{m}^2 \text{ g}^{-1}$)	CrO_4^{2-}			$\text{Cr}_2\text{O}_7^{2-}$		
			PLQY (%)	K_{SV} (M^{-1})	LOD (nM)	Q_{max} (mol mol ⁻¹)	K_{SV} (M^{-1})	LOD (nM)
Th-BCTPE-1	34.1	188	50.53	$2.4(1) \times 10^5$	9.0	1.58	$4.6(3) \times 10^5$	4.6
Th-BCTPE-2	64.7	316	53.07	$1.30(7) \times 10^5$	159	1.22	$2.222(9) \times 10^5$	94

spectrum of **Th-BCTPE-1** and the absorption spectrum of Cr(vi) is greater than that of **Th-BCTPE-2**, which makes **Th-BCTPE-1** as a more sensitive sensor for Cr(vi) detections.

The high sensing efficacy, low LOD, and excellent stability of **Th-BCTPE-1** make it well-suited for the practical application of Cr(vi) sensing (Fig. S10†). To evaluate its potential applicability to real-world conditions, the interfering effects from the environmentally relevant cations and anions were examined by dispersing finely ground **Th-BCTPE-1** in $M(NO_3)_x$ ($M = Al^{3+}$, Cr^{3+} , Mg^{2+} , Ca^{2+} , Sr^{2+} , Cu^{2+} , Zn^{2+} , Mn^{2+} , Ni^{2+} , or K^+ , 2 mM) and Na_xL solutions ($L = F^-$, Cl^- , Br^- , I^- , IO_3^- , NO_3^- , HCO_3^- , SO_4^{2-} , BO_3^{3-} , $Cr_2O_7^{2-}$, CrO_4^{2-} , 2 mM) (Fig. 6a).

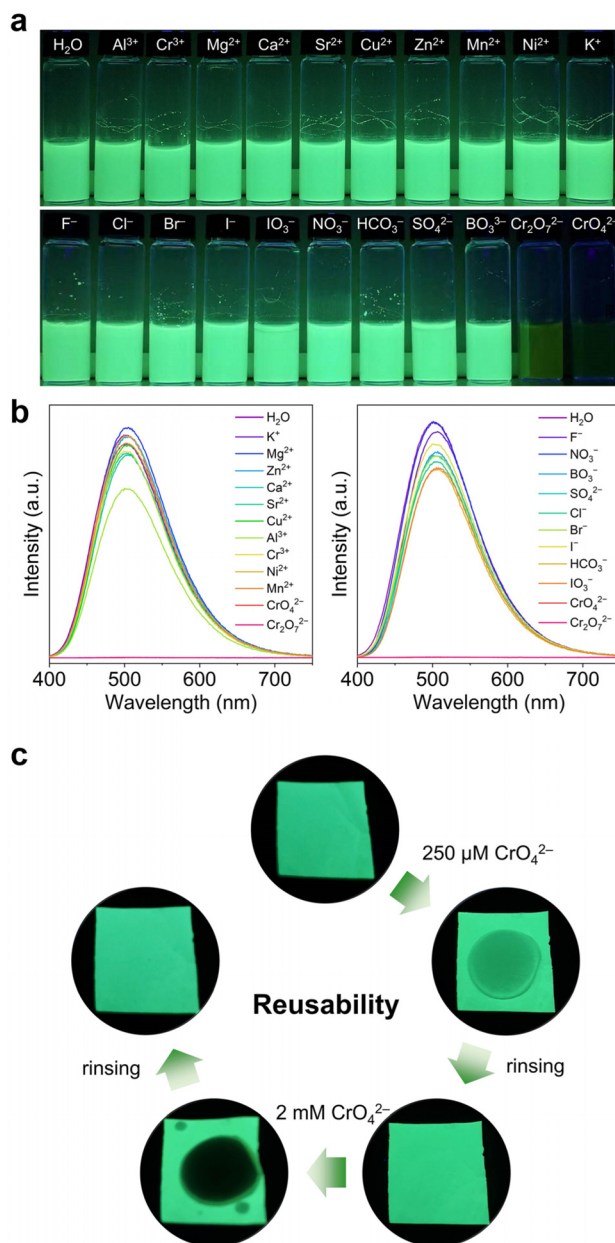


Fig. 6 (a) Photographs of **Th-BCTPE-1** immersed in different cation and anion solutions under UV irradiation. (b) Photoluminescence spectra of **Th-BCTPE-1** immersed in different cation and anion solutions. (c) Photographs of a **Th-BCTPE-1@PVDF** membrane showing its excellent reusability.

BO_3^{3-} , $Cr_2O_7^{2-}$, and CrO_4^{2-} , 2 mM) (Fig. 6a). As shown in Fig. 6b, the luminescence of **Th-BCTPE-1** was completely quenched by CrO_4^{2-} and $Cr_2O_7^{2-}$ with a ratio of 99.84% and 99.91%, respectively. In contrast, minor to moderate emission reductions (−3.52% to 23.62%) occurred upon immersing **Th-BCTPE-1** in interfering cation or anion solutions. These results are testaments to the excellent sensing selectivity of **Th-BCTPE-1** over the environmentally relevant cationic and anionic species.⁵⁸ To achieve the facile and on-site sensing of the Cr(vi) oxyanion, we further fabricated the MOF-based polyvinylidene fluoride (PVDF) membrane by dispersing finely ground **Th-BCTPE-1** in PVDF.^{59,60} As shown in Fig. 6c, the as-prepared **Th-BCTPE-1@PVDF** membrane shows green luminescence under a 365 nm UV lamp.

Upon applying CrO_4^{2-} or $Cr_2O_7^{2-}$ solution, a dark spot was observed and its darkness increased with the increasing Cr(vi) concentration. More strikingly, the quenched luminescence of **Th-BCTPE-1@PVDF** can be recovered by simply rinsing the membrane with DI water, indicating the excellent reusability of **Th-BCTPE-1@PVDF**.

Conclusions

In summary, LMOFs have been considered a promising material platform for sensing carcinogenic chromate and dichromate. Therefore, unravelling the correlation between the MOF structure and the sensing efficacy is essential to the rational design of high-performance MOF-based sensors. In this work, a simple synthetic modulation approach has given rise to two luminescent Th-MOFs, **Th-BCTPE-1** and **Th-BCTPE-2**, which are built from similar hexanuclear SBUs and identical BCTPE²⁺ linkers. Such polymorphism of Th-MOFs in terms of topology allows for elucidating how the structure of MOF, in isolation, influences the sensing efficacy of Cr(vi) oxyanions. Indeed, we find that the UiO-type MOF **Th-BCTPE-1** has greater K_{SV} and lower LOD for both CrO_4^{2-} and $Cr_2O_7^{2-}$ than the more porous **Th-BCTPE-2**. **Th-BCTPE-1** features the second highest K_{SV} of CrO_4^{2-} ($2.84(4) \times 10^5$) among all MOF-based Cr(vi) sensors. Moreover, the sensing efficacies of CrO_4^{2-} and $Cr_2O_7^{2-}$ have proved to be positively correlated with the adsorption capacity and degree of the inner filter effect; the higher ones for **Th-BCTPE-1** render its luminophores more accessible to Cr(vi) oxyanions. In contrast, other physicochemical properties, including porosity, BET surface area, and photoluminescence quantum yield, appear to play a much less significant role in determining the sensing efficacy. In addition, **Th-BCTPE-1** exhibits excellent sensing selectivity for CrO_4^{2-} and $Cr_2O_7^{2-}$, which is a key merit for the deployment of LMOFs in environmentally related conditions.

Experimental section

Synthesis

Th-BCTPE-1. A mixture of $Th(NO_3)_4 \cdot 6H_2O$ (4.7 mg, 0.008 mmol), 4,4'-(1,2-diphenylethene-1,2-diyl) dibenzoic acid

(H₂BCTPE, 1.7 mg, 0.004 mmol), DMF (0.308 mL), MeOH (0.2 mL), and trifluoroacetic acid (0.04 mL) in a capped vial was heated at 80 °C for 48 h. Colourless octahedral crystals were obtained, filtered, washed with MeOH and Et₂O, and dried at room temperature. The pH values before and after crystallization of **Th-BCTPE-1** were 0.91 and 5.71, respectively. Yield: 47% based on H₂BCTPE. Anal. calcd for [Th₆(μ₃-OH)₄(μ₃-O)₄(BCTPE)₆(H₂O)₆]·(C₃H₇NO)₁₈·(H₂O)₉, C₂₂₂H₂₆₈N₁₈Th₆O₆₅, C, 47.44%; H, 4.81%; N, 4.49%. Found: C, 47.08%; H, 4.48%; N, 4.77%.

Th-BCTPE-2. A mixture of Th(NO₃)₄·6H₂O (4.7 mg, 0.008 mmol), 4,4'-(1,2-diphenylethene-1,2-diyl)dibenzoic acid (H₂BCTPE, 0.9 mg, 0.002 mmol), DMF (0.879 mL), and concentrated nitric acid (0.025 mL) in a capped vial was heated at 120 °C for 96 h. Colourless needle crystals were obtained, filtered, washed with MeOH and Et₂O, and dried at room temperature. The pH values before and after the crystallization of **Th-BCTPE-2** were 1.12 and 5.33, respectively. Yield: 44% based on H₂BCTPE. Anal. calcd for [Th₆(μ₃-OH)₄(μ₃-O)₄(BCTPE)₅(HCOO)₂(H₂O)₆]·(C₃H₇NO)₂₆·(H₂O)₃₂, C₂₂₀H₃₅₄N₂₆Th₆O₉₆, C, 42.00%; H, 5.67%; N, 5.79%. Found: C, 41.51%; H, 5.33%; N, 5.99%.

Characterization

Single-crystal X-ray diffraction data were collected on a Bruker D8-Venture single-crystal X-ray diffractometer equipped with an IP-S 3.0 microfocus X-ray source (Mo-Kα radiation, $\lambda = 0.71073 \text{ \AA}$) and a CMOS detector. The data frames were collected using the APEX3 program and processed using the SAINT routine. The empirical absorption correction was applied using the SADABS program.⁶¹ The structure was solved by intrinsic phasing with ShelXT and refined with ShelXL using OLEX2.^{62–64} All the non-H atoms were subjected to anisotropic refinement by a full-matrix program. Contributions to scattering due to these highly disordered solvent molecules were removed using the SQUEEZE routine of PLATON.⁴⁰ Structures were then refined again using the data generated. Crystal data and details of the data collection are given in Table S1.† Powder X-ray diffraction (PXRD) data were collected from 2 to 40° with a step of 0.02° on a Bruker D8 Advance diffractometer with Cu Kα radiation ($\lambda = 1.54178 \text{ \AA}$). The calculated PXRD pattern was produced from the CIFs using the Mercury 1.4.2 program. The N₂ adsorption isotherms were obtained at 77 K by using a Micromeritics ASAP 2020. The freshly prepared Th-MOFs were soaked in 20 mL of DCM three times over 1 h (20 min each) and subsequently immersed in 20 mL *n*-hexane three times over 1 h (20 min each). The excitation and luminescence spectra were collected on an Edinburgh Instruments FS5 fluorescence spectrometer. The photoluminescence lifetimes and quantum yields were obtained on an Edinburgh Instruments FLS 980 spectrometer. Scanning electron microscopy (SEM) images and energy-dispersive spectroscopy (EDS) data were collected on a Zeiss Merlin Compact LEO 1530 VP scanning electron microscope with the energy of the electron beam being 15 kV. Thermalgravimetric analysis (TGA) was carried out on a NETZSCH STA 449 F3 Jupiter instrument in

the range of 30–800 °C under a nitrogen flow at a heating rate of 10 °C min⁻¹.

Author contributions

J. L. conceived and designed the research. Z. J. L., Y. J., and X. L. synthesized the materials and performed the luminescence study. Z. J. L. and Y. L. solved the crystal structures. X. L. W. performed the BET study. J. L., Z. J. L., J. Q., J. Q. W., Z. H. Z., M. Y. H., and L. Z. analysed the data and wrote the manuscript. All authors have given approval to the manuscript.

Conflicts of interest

The authors declare no competing financial interests.

Acknowledgements

This work was supported by the National Natural Science Foundation of China (22076196, U22B20139, 21906163, and 21876182), the Strategic Priority Research Program of the Chinese Academy of Sciences (XDA21000000), and the K. C. Wong Education Foundation (GJTD-2018-10).

References

- 1 B. Dhal, H. N. Thatoi, N. N. Das and B. D. Pandey, Chemical and microbial remediation of hexavalent chromium from contaminated soil and mining/metallurgical solid waste: A review, *J. Hazard. Mater.*, 2013, **250–251**, 272–291.
- 2 S. S. Galley, A. A. Arico, T.-H. Lee, X. Deng, Y.-X. Yao, J. M. Sperling, V. Proust, J. S. Storbeck, V. Dobrosavljevic, J. N. Neu, T. Siegrist, R. E. Baumbach, T. E. Albrecht-Schmitt, N. Kaltsoyannis and N. Lanatà, Uncovering the Origin of Divergence in the CsM(CrO₄)₂ (M = La, Pr, Nd, Sm, Eu; Am) Family through Examination of the Chemical Bonding in a Molecular Cluster and by Band Structure Analysis, *J. Am. Chem. Soc.*, 2018, **140**, 1674–1685.
- 3 USDOE Hanford Site First Five Year Review Report, *USDOE Hanford Site First Five Year Review Report*, DOE-RL-2011-56, 2001.
- 4 P. E. Dresel, M. J. Truex and M. D. Sweeney, *Review of Techniques to Characterize the Distribution of Chromate Contamination in the Vadose Zone of the 100 Areas at the Hanford Site*, United States, 2007.
- 5 A. M. Zayed and N. Terry, Chromium in the environment: factors affecting biological remediation, *Plant Soil*, 2003, **249**, 139–156.
- 6 P. Izak, P. Hrma, B. W. Arey and T. J. Plaisted, Effect of feed melting, temperature history, and minor component

addition on spinel crystallization in high-level waste glass, *J. Non-Cryst. Solids*, 2001, **289**, 17–29.

7 H. Fei, C. H. Pham and S. R. J. Oliver, Anion exchange of the cationic layered material $[\text{Pb}_2\text{F}_2]^{2+}$, *J. Am. Chem. Soc.*, 2012, **134**, 10729–10732.

8 H. Fei, M. R. Bresler and S. R. J. Oliver, A New Paradigm for Anion Trapping in High Capacity and Selectivity: Crystal-to-Crystal Transformation of Cationic Materials, *J. Am. Chem. Soc.*, 2011, **133**, 11110–11113.

9 H. Yang and H. Fei, Exfoliation of a two-dimensional cationic inorganic network as a new paradigm for high-capacity Cr^{VI} -anion capture, *Chem. Commun.*, 2017, **53**, 7064–7067.

10 X. Chen, X. Dai, R. Xie, J. Li, A. Khayambashi, L. Xu, C. Yang, N. Shen, Y. Wang, L. He, Y. Zhang, C. Xiao, Z. Chai and S. Wang, Chromate separation by selective crystallization, *Chin. Chem. Lett.*, 2020, **31**, 1974–1977.

11 H. Fei, C. S. Han, J. C. Robins and S. R. J. Oliver, A Cationic Metal–Organic Solid Solution Based on $\text{Co}^{(\text{II})}$ and $\text{Zn}^{(\text{II})}$ for Chromate Trapping, *Chem. Mater.*, 2013, **25**, 647–652.

12 J. G. Farmer, R. P. Thomas, M. C. Graham, J. S. Geelhoed, D. G. Lumsdon and E. Paterson, Chromium speciation and fractionation in ground and surface waters in the vicinity of chromite ore processing residue disposal sites, *J. Environ. Monit.*, 2002, **4**, 235–243.

13 Z. Hu, B. J. Deibert and J. Li, Luminescent metal–organic frameworks for chemical sensing and explosive detection, *Chem. Soc. Rev.*, 2014, **43**, 5815–5840.

14 Y. Bai, Y. Dou, L.-H. Xie, W. Rutledge, J.-R. Li and H.-C. Zhou, Zr-based metal–organic frameworks: design, synthesis, structure, and applications, *Chem. Soc. Rev.*, 2016, **45**, 2327–2367.

15 Q. Wang, Q. Gao, A. M. Al-Enizi, A. Nafady and S. Ma, Recent advances in MOF-based photocatalysis: environmental remediation under visible light, *Inorg. Chem. Front.*, 2020, **7**, 300–339.

16 X. Wang, P. C. Lan and S. Ma, Metal–Organic Frameworks for Enzyme Immobilization: Beyond Host Matrix Materials, *ACS Cent. Sci.*, 2020, **6**, 1497–1506.

17 Y. Ye, S. Xian, H. Cui, K. Tan, L. Gong, B. Liang, T. Pham, H. Pandey, R. Krishna, P. C. Lan, K. A. Forrest, B. Space, T. Thonhauser, J. Li and S. Ma, Metal–Organic Framework Based Hydrogen-Bonding Nanotrap for Efficient Acetylene Storage and Separation, *J. Am. Chem. Soc.*, 2022, **144**, 1681–1689.

18 Z. Niu, Z. Fan, T. Pham, G. Verma, K. A. Forrest, B. Space, P. K. Thallapally, A. M. Al-Enizi and S. Ma, Self-Adjusting Metal–Organic Framework for Efficient Capture of Trace Xenon and Krypton, *Angew. Chem. Int. Ed.*, 2022, **61**, 1433–7851.

19 W. Liu, Y. Wang, Z. Bai, Y. Li, Y. Wang, L. Chen, L. Xu, J. Diwu, Z. Chai and S. Wang, Hydrolytically Stable Luminescent Cationic Metal Organic Framework for Highly Sensitive and Selective Sensing of Chromate Anions in Natural Water Systems, *ACS Appl. Mater. Interfaces*, 2017, **9**, 16448–16457.

20 Z.-J. Li, M. Lei, H. Bao, Y. Ju, H. Lu, Y. Li, Z.-H. Zhang, X. Guo, Y. Qian, M.-Y. He, J.-Q. Wang, W. Liu and J. Lin, A cationic thorium–organic framework with triple single-crystal-to-single-crystal transformation peculiarities for ultrasensitive anion recognition, *Chem. Sci.*, 2021, **12**, 15833–15842.

21 Z.-J. Li, X. Wang, L. Zhu, Y. Ju, Z. Wang, Q. Zhao, Z.-H. Zhang, T. Duan, Y. Qian, J.-Q. Wang and J. Lin, Hydrolytically Stable Zr-Based Metal–Organic Framework as a Highly Sensitive and Selective Luminescent Sensor of Radionuclides, *Inorg. Chem.*, 2022, **61**, 7467–7476.

22 Z.-H. Zhu, Z. Ni, H.-H. Zou, G. Feng and B. Z. Tang, Smart Metal–Organic Frameworks with Reversible Luminescence/Magnetic Switch Behavior for HCl Vapor Detection, *Adv. Funct. Mater.*, 2021, **31**, 2106925.

23 X. Li, H. Xu, F. Kong and R. Wang, A Cationic Metal–Organic Framework Consisting of Nanoscale Cages: Capture, Separation, and Luminescent Probing of $\text{Cr}_2\text{O}_7^{2-}$ through a Single-Crystal to Single-Crystal Process, *Angew. Chem., Int. Ed.*, 2013, **52**, 13769–13773.

24 B. Parmar, Y. Rachuri, K. K. Bisht and E. Suresh, Mixed-Ligand LMOF Fluorosensors for Detection of $\text{Cr}(\text{vi})$ Oxyanions and $\text{Fe}^{3+}/\text{Pd}^{2+}$ Cations in Aqueous Media, *Inorg. Chem.*, 2017, **56**, 10939–10949.

25 F.-Y. Yi, J.-P. Li, D. Wu and Z.-M. Sun, A Series of Multifunctional Metal–Organic Frameworks Showing Excellent Luminescent Sensing, Sensitization, and Adsorbent Abilities, *Chem. – Eur. J.*, 2015, **21**, 11475–11482.

26 C. Zhang, L. Sun, Y. Yan, H. Shi, B. Wang, Z. Liang and J. Li, A novel photo- and hydrochromic europium metal–organic framework with good anion sensing properties, *J. Mater. Chem. C*, 2017, **5**, 8999–9004.

27 T.-Y. Gu, M. Dai, D. J. Young, Z.-G. Ren and J.-P. Lang, Luminescent $\text{Zn}^{(\text{II})}$ Coordination Polymers for Highly Selective Sensing of $\text{Cr}^{(\text{III})}$ and $\text{Cr}^{(\text{VI})}$ in Water, *Inorg. Chem.*, 2017, **56**, 4668–4678.

28 R. Lv, J. Wang, Y. Zhang, H. Li, L. Yang, S. Liao, W. Gu and X. Liu, An amino-decorated dual-functional metal–organic framework for highly selective sensing of $\text{Cr}^{(\text{III})}$ and $\text{Cr}^{(\text{VI})}$ ions and detection of nitroaromatic explosives, *J. Mater. Chem. A*, 2016, **4**, 15494–15500.

29 Y. Lin, X. Zhang, W. Chen, W. Shi and P. Cheng, Three Cadmium Coordination Polymers with Carboxylate and Pyridine Mixed Ligands: Luminescent Sensors for Fe-III and Cr-VI Ions in an Aqueous Medium, *Inorg. Chem.*, 2017, **56**, 11768–11778.

30 Z.-J. Li, X. Guo, J. Qiu, H. Lu, J.-Q. Wang and J. Lin, Recent advances in the applications of thorium-based metal–organic frameworks and molecular clusters, *Dalton Trans.*, 2022, **51**, 7376–7389.

31 K. Lv, S. Fichter, M. Gu, J. März and M. Schmidt, An updated status and trends in actinide metal–organic frameworks (An-MOFs): From synthesis to application, *Coord. Chem. Rev.*, 2021, **446**, 214011.

32 E. A. Dolgopolova, O. A. Ejegbabwo, C. R. Martin, M. D. Smith, W. Setyawan, S. G. Karakalos, C. H. Henager,

H.-C. zur Loyer and N. B. Shustova, Multifaceted Modularity: A Key for Stepwise Building of Hierarchical Complexity in Actinide Metal–Organic Frameworks, *J. Am. Chem. Soc.*, 2017, **139**, 16852–16861.

33 E. A. Dolgopolova, A. M. Rice and N. B. Shustova, Actinide-Based MOFs: a Middle Ground in Solution and Solid-State Structural Motifs, *Chem. Commun.*, 2018, **54**, 6472–6483.

34 O. A. Ejegbawo, C. R. Martin, O. A. Olorunfemi, G. A. Leith, R. T. Ly, A. M. Rice, E. A. Dolgopolova, M. D. Smith, S. G. Karakalos, N. Birkner, B. A. Powell, S. Pandey, R. J. Koch, S. T. Misture, H.-C. z. Loyer, S. R. Phillipot, K. S. Brinkman and N. B. Shustova, Thermodynamics and Electronic Properties of Heterometallic Multinuclear Actinide-Containing Metal–Organic Frameworks with “Structural Memory”, *J. Am. Chem. Soc.*, 2019, **141**, 11628–11640.

35 C. R. Martin, G. A. Leith, P. Kittikhunnatham, K. C. Park, O. A. Ejegbawo, A. Mathur, C. R. Callahan, S. L. Desmond, M. R. Keener, F. Ahmed, S. Pandey, M. D. Smith, S. R. Phillipot, A. B. Greytak and N. B. Shustova, Heterometallic Actinide-Containing Photoresponsive Metal–Organic Frameworks: Dynamic and Static Tuning of Electronic Properties, *Angew. Chem., Int. Ed.*, 2021, **60**, 8072–8080.

36 Z.-J. Li, S. Guo, H. Lu, Y. Xu, Z. Yue, L. Weng, X. Guo, J. Lin and J.-Q. Wang, Unexpected Structural Complexity of Thorium Coordination Polymers and Polyoxo Cluster Built from Simple Formate Ligands, *Inorg. Chem. Front.*, 2020, **7**, 260–269.

37 Y. Ju, Z.-J. Li, H. Lu, Z. Zhou, Y. Li, X.-L. Wu, X. Guo, Y. Qian, Z.-H. Zhang, J. Lin, J.-Q. Wang and M.-Y. He, Interpenetration Control in Thorium Metal–Organic Frameworks: Structural Complexity toward Iodine Adsorption, *Inorg. Chem.*, 2021, **60**, 5617–5626.

38 Z.-J. Li, Y. Ju, Z. Zhang, H. Lu, Y. Li, N. Zhang, X.-L. Du, X. Guo, Z.-H. Zhang, Y. Qian, M.-Y. He, J.-Q. Wang and J. Lin, Unveiling the Unique Roles of Metal Coordination and Modulator in the Polymorphism Control of Metal–Organic Frameworks, *Chem. – Eur. J.*, 2021, **27**, 17586–17594.

39 Z.-J. Li, S. Guo, H. Lu, Y. Xu, Z. Yue, L. Weng, X. Guo, J. Lin and J.-Q. Wang, Unexpected structural complexity of thorium coordination polymers and polyoxo cluster built from simple formate ligands, *Inorg. Chem. Front.*, 2020, **7**, 260–269.

40 A. Spek, PLATON SQUEEZE: a tool for the calculation of the disordered solvent contribution to the calculated structure factors, *Acta Crystallogr., Sect. C: Struct. Chem.*, 2015, **71**, 9–18.

41 X.-G. Liu, C.-L. Tao, H.-Q. Yu, B. Chen, Z. Liu, G.-P. Zhu, Z. Zhao, L. Shen and B. Z. Tang, A new luminescent metal–organic framework based on dicarboxyl-substituted tetraphenylethene for efficient detection of nitro-containing explosives and antibiotics in aqueous media, *J. Mater. Chem. C*, 2018, **6**, 2983–2988.

42 N. B. Shustova, B. D. McCarthy and M. Dincă, Turn-On Fluorescence in Tetraphenylethylene-Based Metal–Organic Frameworks: An Alternative to Aggregation-Induced Emission, *J. Am. Chem. Soc.*, 2011, **133**, 20126–20129.

43 D. F. Sava Gallis, L. E. S. Rohwer, M. A. Rodriguez and T. M. Nenoff, Efficient Photoluminescence via Metal–Ligand Alteration in a New MOFs Family, *Chem. Mater.*, 2014, **26**, 2943–2951.

44 C. Peng, X. Song, J. Yin, G. Zhang and H. Fei, Intrinsic White-Light-Emitting Metal–Organic Frameworks with Structurally Deformable Secondary Building Units, *Angew. Chem., Int. Ed.*, 2019, **58**, 7818–7822.

45 Z. Wei, Z.-Y. Gu, R. K. Arvapally, Y.-P. Chen, R. N. McDougald, J. F. Ivy, A. A. Yakovenko, D. Feng, M. A. Omary and H.-C. Zhou, Rigidifying Fluorescent Linkers by Metal–Organic Framework Formation for Fluorescence Blue Shift and Quantum Yield Enhancement, *J. Am. Chem. Soc.*, 2014, **136**, 8269–8276.

46 M. H. Gehlen, The centenary of the Stern–Volmer equation of fluorescence quenching: From the single line plot to the SV quenching map, *J. Photochem. Photobiol. C*, 2020, **42**, 100338.

47 B. Parmar, K. K. Bisht, Y. Rachuri and E. Suresh, Zn(ii)/Cd (ii) based mixed ligand coordination polymers as fluorosensors for aqueous phase detection of hazardous pollutants, *Inorg. Chem. Front.*, 2020, **7**, 1082–1107.

48 Y.-J. Yang, Y.-H. Li, D. Liu and G.-H. Cui, A dual-responsive luminescent sensor based on a water-stable Cd(ii)-MOF for the highly selective and sensitive detection of acetylacetone and Cr₂O₇²⁻ in aqueous solutions, *CrystEngComm*, 2020, **22**, 1166–1175.

49 M. B. Luo, Y. Y. Xiong, H. Q. Wu, X. F. Feng, J. Q. Li and F. Luo, The MOF+ Technique: A Significant Synergic Effect Enables High Performance Chromate Removal, *Angew. Chem., Int. Ed.*, 2017, **56**, 16376–16379.

50 S. R. J. Oliver, Cationic inorganic materials for anionic pollutant trapping and catalysis, *Chem. Soc. Rev.*, 2009, **38**, 1868–1881.

51 Z.-J. Li, Y. Ju, B. Yu, X. Wu, H. Lu, Y. Li, J. Zhou, X. Guo, Z.-H. Zhang, J. Lin, J.-Q. Wang and S. Wang, Modulated synthesis and isoreticular expansion of Th-MOFs with record high pore volume and surface area for iodine adsorption, *Chem. Commun.*, 2020, **56**, 6715–6718.

52 X. Chen, Y. Yu, C. Yang, J. Yin, X. Song, J. Li and H. Fei, Fabrication of Robust and Porous Lead Chloride-Based Metal–Organic Frameworks toward a Selective and Sensitive Smart NH₃ Sensor, *ACS Appl. Mater. Interfaces*, 2021, **13**, 52765–52774.

53 S. E. Crawford, J. E. Ellis, P. R. Ohodnicki and J. P. Baltrus, Influence of the Anionic Zinc-Adeninate Metal–Organic Framework Structure on the Luminescent Detection of Rare Earth Ions in Aqueous Streams, *ACS Appl. Mater. Interfaces*, 2021, **13**, 7268–7277.

54 H. Yuan, N. Li, W. Fan, H. Cai and D. Zhao, Metal–Organic Framework Based Gas Sensors, *Adv. Sci.*, 2021, **9**, 2104374.

55 A. S. Tanwar, L. R. Adil, M. A. Afroz and P. K. Iyer, Inner Filter Effect and Resonance Energy Transfer Based Attogram Level Detection of Nitroexplosive Picric Acid

Using Dual Emitting Cationic Conjugated Polyfluorene, *ACS Sens.*, 2018, **3**, 1451–1461.

56 P. Daga, S. Sarkar, P. Majee, D. K. Singha, S. Hui, P. Mahata and S. K. Mondal, A selective detection of nanomolar-range noxious anions in water by a luminescent metal-organic framework, *Mater. Adv.*, 2021, **2**, 985–995.

57 L. Qiu, Z. Ma, P. Li, X. Hu, C. Chen, X. Zhu, M. Liu, Y. Zhang, H. Li and S. Yao, Sensitive and selective detection of chromium(vi) based on two-dimensional luminescence metal organic framework nanosheets via the mechanism integrating chemical oxidation-reduction and inner filter effect, *J. Hazard. Mater.*, 2021, **419**, 126443.

58 X. Wang, Z.-J. Li, Y. Ju, X. Li, J. Qian, M.-Y. He, J.-Q. Wang, Z.-H. Zhang and J. Lin, A MOF-based luminometric sensor for ultra-sensitive and highly selective detection of chromium oxyanions, *Talanta*, 2023, **252**, 123894.

59 C. Liang, S. Zhang, L. Cheng, J. Xie, F. Zhai, Y. He, Y. Wang, Z. Chai and S. Wang, Thermoplastic Membranes Incorporating Semiconductive Metal–Organic Frameworks: An Advance on Flexible X-ray Detectors, *Angew. Chem., Int. Ed.*, 2020, **59**, 11856–11860.

60 M. S. Denny Jr., J. C. Moreton, L. Benz and S. M. Cohen, Metal-organic frameworks for membrane-based separations, *Nat. Rev. Mater.*, 2016, **1**, 16078.

61 G. M. Sheldrick, *SADABS, program for empirical absorption correction of area detector data*, University of Göttingen, Göttingen, Germany, 1996.

62 G. M. Sheldrick, *SHELXT – Integrated space-group and crystal-structure determination*, *Acta Crystallogr., Sect. A: Found. Adv.*, 2015, **71**, 3–8.

63 G. M. Sheldrick, Crystal structure refinement with *SHELXL*, *Acta Crystallogr., Sect. C: Struct. Chem.*, 2015, **71**, 3–8.

64 O. V. Dolomanov, L. J. Bourhis, R. J. Gildea, J. A. K. Howard and H. Puschmann, *OLEX2: a complete structure solution, refinement and analysis program*, *J. Appl. Crystallogr.*, 2009, **42**, 339–341.